Journal of Controlled Release 358 (2023) 718–728

Contents lists available at ScienceDirect

Journal of Controlled Release

journal homepage: www.elsevier.com/locate/jconrel

Programmed antigen capture-harnessed dendritic cells by margination-hitchhiking lung delivery

Thi My Hue Huynh [a], Bhanu Nirosha Yalamandala [a], Min-Ren Chiang [a], Wei-Han Weng [a], Chien-Wen Chang [a], Wen-Hsuan Chiang [b], Lun-De Liao [c], Yu-Chen Liu [d], Shang-Hsiu Hu [a,*]

[a] Department of Biomedical Engineering and Environmental Sciences, National Tsing Hua University, Hsinchu 300044, Taiwan
[b] Department of Chemical Engineering, National Chung Hsing University, Taichung 402, Taiwan
[c] Institute of Biomedical Engineering and Nanomedicine, National Health Research Institutes, Miaoli County 35053, Taiwan
[d] Laboratory for Human Immunology (Single Cell Genomics), WPI Immunology Frontier Research Center, Osaka University, Japan

ARTICLE INFO

Keywords:
Red blood cell
Hitchhiking
Antigen capture
Immune therapy
Lung metastases

ABSTRACT

Adoptive T cells and immunotherapy suppress the most destructive metastatic tumors and prevent tumor recurrence by inducing T lymphocytes. However, the heterogeneity and immune privilege of invasive metastatic clusters often reduce immune cell infiltration and therapeutic efficacy. Here, the red blood cells (RBC)-hitchhiking mediated lung metastasis delivery of multi-grained iron oxide nanostructures (MIO) programming the antigen capture, dendritic cell harnessing, and T cell recruitment is developed. MIO is assembled to the surface of RBCs by osmotic shock-mediated fusion, and reversible interactions enable the transfer of MIO to pulmonary capillary endothelial cells by intravenous injection by squeezing RBCs at the pulmonary microvessels. RBC-hitchhiking delivery revealed that >65% of MIOs co-localized in tumors rather than normal tissues. In alternating magnetic field (AMF)-mediated magnetic lysis, MIO leads to the release of tumor-associated antigens, namely neoantigens and damage-associated molecular patterns. It also acted as an antigen capture agent-harnessed dendritic cells delivers these antigens to lymph nodes. By utilizing site-specific targeting, erythrocyte hitchhiker-mediated delivery of MIO to lung metastases improves survival and immune responses in mice with metastatic lung tumors.

1. Introduction

Cancer immunotherapy boosts the immune system and primes T cells to recognize and fight cancer cells, potentially suppressing tumors and inducing immune memory [1,2]. Despite recent advances in immunotherapy, the poor vascularization and low presence of tumor-associated antigens at metastases of numerous invading clusters (usually smaller than <100 mm3) deteriorates the plight of weakening physical contact between T cells and cancer cells at the early metastasis stage [3–5]. Furthermore, immune privilege arises from the recognition of T cells by cancer cells, leading to the escape of T cell attacks [6,7].

To overcome this obstacle, a simple strategy is to collect functional reagents in target organs and then guide cancer cell apoptosis to release secondary tumor antigens and promote T cell induction. In this regard, a neovascular-targeted delivery system exhibits accumulation in early metastases, but clinically low tumor suppression is attributed to the accumulation of stromal thylakoids [8–10]. Another approach is to engineer functional agents onto a specific cell to hitchhike into the target organ [11–13]. For example, RBC can squeeze through capillaries with a much narrower diameter and recover their original shape rapidly owing to their flexibility [14,15]; thus, therapeutic agents, such as liposomes or pro-drugs [16,17], can be transferred to lung metastasis *via* RBC hitchhiking [18,19]. Besides that, due to the feature of RBC, it can be supplied for drug delivery as their natural lung targetability. As documented in the literatures, RBCs squeezed through the lung capillaries and transferred cargo to pulmonary capillary endothelial cells [20–22]. Furthermore, cell-hitchhiking drug-carrying particles enhance nanoparticle delivery capabilities (*e.g.*, targeting and circulation) and increase their efficacy in clinical trials, while reducing toxic side effects [23,24]. RBC are ideal candidates to meet all the requirements of drug delivery systems, such as prolongation of systemic circulation time, are endogenous cells with high biocompatibility and low immunogenicity [25–28].

In addition to targeting, immune regulation and tumor infiltrating

* Corresponding author.
E-mail address: shhu@mx.nthu.edu.tw (S.-H. Hu).

https://doi.org/10.1016/j.jconrel.2023.05.028
Received 13 January 2023; Received in revised form 18 April 2023; Accepted 19 May 2023

lymphocytes are important issues in metastatic immunotherapy [29–31]. Magnetic hyperthermia *via* iron oxide nanoparticles (IO) involves destruction of tumors by localized heating up to 41–46 °C, which leads to the killing of cancer cells or permanent cell damage *via* apoptotic or necrotic pathways [32–36]. Efficient apoptosis or necrosis can activate tumor-associated antigens and promote the recruitment of T cells [37–42]. In particular, IO has been reported as an antigen carrier and adjuvant [43–45], both of which promote efficient antigen presentation and antigen-specific approaches to activate downstream immune processes [46,47].

Here, a multi-grained iron oxide nanostructures (MIO) assembled onto RBC (MIO@RBC) that combines the features of RBC hitchhiking and immunomodulator was developed for lung metastasis targeting and hyperthermia at tumor (Fig. 1a). After hitchhiking to the lung, MIO penetrates into lung metastases through uptake by alveolar luminal endothelial cells and leukocytes, which then absorb energy and cause cancer cell apoptosis (Fig. 1b). As it exhibits multi-domains of magnetic crystalline, the frictional heat on MIOs can be generated by an alternating magnetic field (AFM) *via* the magnetic spin flipping (Néel relaxation) and particle rotation (Brownian relaxation) at moderate intensity and operating frequency. In tumors, induced heat further causes cancer to invoke apoptosis to release tumor-associated antigens. In addition, MIO acts as an antigen capture agent to deliver neoantigens and damage-associated molecular patterns to lymph nodes, contributing to efficient T cell recruitment and immunotherapy (Fig. 1b). The large amount of MIOs disrupts the cell-cell interactions at tumor, actuating T cell infiltration. The versatile MIO@RBC is an outstanding immune modulator for improving immune response at lung metastases and activating T cells. In addition to RBC hitchhiking strategy for iron oxide nanoparticles to lung, the innovations of this study are as follows. (1) The multiple domains of the MIO can generate intense heat remotely through an alternating magnetic field (AFM). (2) MIO acts as an antigen capture agent to deliver neoantigens and damage-associated molecular patterns to lymph nodes. (3) Intercellular interactions at the tumor may be disrupted, promoting T cell infiltration. The multifunctional MIO@RBC is an excellent immunomodulator that improves the immune response and activates T cells in lung metastases.

2. Material and method

2.1. Synthesis of multi-grained Iron oxide nanostructures (MIOs)

Multi-Grained Iron Oxide Nanostructures (MIOs) were fabricated *via* a facile ligand-assisted hydrothermal reaction. In brief, ferric chloride hexahydrate ($FeCl_3{\cdot}6H_2O$, 20 mmol, Sigma-Aldrich) and 0.5 mL of oleylamine (OA, Sigma-Aldrich) was dissolved in 40 mL ethylene glycol solution (EG, anhydrous, 99%, Sigma-Aldrich) and gently stirred at room temperature. Then, 40 mmol of sodium acetate (NaAc, Sigma-Aldrich) was added into the mixture and continuous stirring to obtain a homogeneous brown solution. The homogeneous mixture was transferred to a Teflon-lined stainless-steel autoclave after 1 h stirring for hydrothermal reaction at 200 °C to 240 °C for 6, 12, 18 and 24 h, respectively. After the reaction, the mixture was allowed to cool down to room temperature, and the precipitate was collected in ethanol by centrifugation at 3500 rpm for 10 min. Finally, the unreacted agents were washed away with excess ethanol and DI water 3 times afterwards and stored in ethanol at 4 °C for later use.

2.2. Blood collection and isolation of RBCs

In briefly, whole blood from C57BL/6 mice aged 6 to 8 weeks was collected *via* submandibular vein using a mouse bleeding lancet (Goldenrod animal lancet, 5 mm, USA) and heparin tube (Lithium Heparin, USA) as an anti-coagulant. First, RBC compartment separated from the serum, plasma, and buffy coat by centrifuging at 2852 rpm for 10 min at 4 °C. The isolated RBC was then washed with cold PBS three times before their final resuspension at a concentration of 20% hematocrit in PBS (defined as stock solution of RBC). RBC solution was reserved at 4 °C for no longer than 42 days [48]. Freshly processed RBC was used for every experiment in this study.

2.3. Binding of MIOs to RBCs

Briefly, RBCs (8×10^{10} cells/ mL) were incubated with MIOs at ratio of 200–500:1 (*v*/v), and then shaken at constant rotation for 5 to 30 min at 4 °C in PBS. MIO@RBC solution was isolated from unabsorbed particles by centrifugation at 100 ×*g* for 5 min at 4 °C, the MIO@RBC

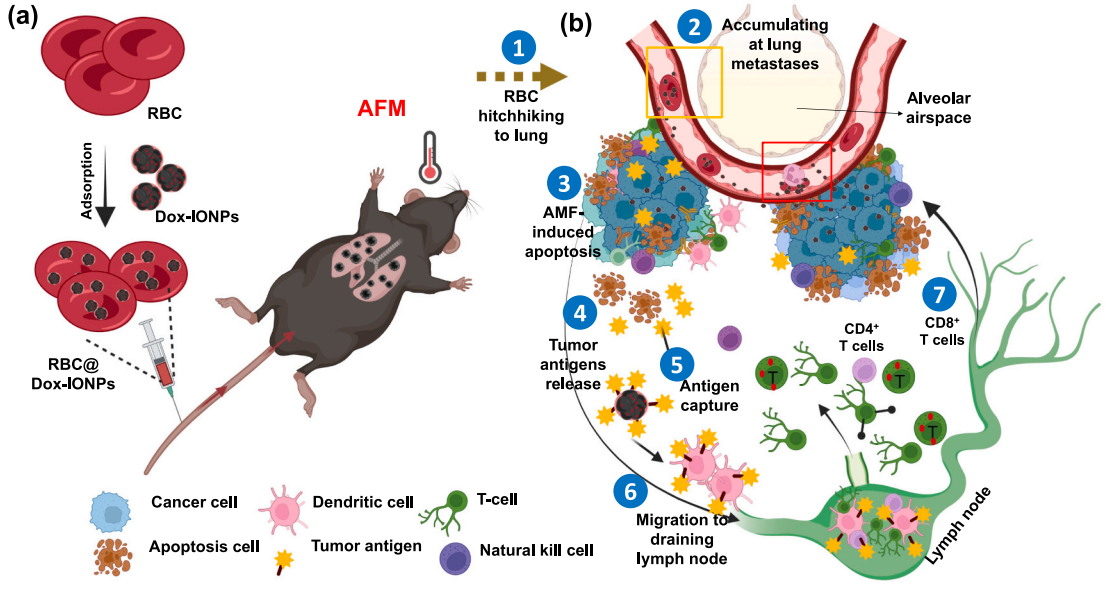

Fig. 1. (a) Schematic illustration of RBC-hitchhiking delivery of MIO to lung metastasis for immune therapy. (b) MIO penetrates into lung metastasis *via* the endothelial cells and leukocyte uptake at aleveolar airspace, and then, absorbs energy and causes cancer cell apoptosis. The frictional heat on MIOs by an alternating magnetic field (AFM) leads the cancer call apoptosis to release of tumor-associated antigens, facilitating to the recruitment of T cells.

solution was washed again with 1 mL of 1× PBS, and then resuspended at 20% (v/v) in 1× PBS, and finally stored at 4 °C for further studies. Coupling efficiency was determined using fluorescence measurements. The percentage of NPs hitchhiked to RBC membrane for different NP-to-RBC ratios was examined by using flow cytometry (BD LSR Analyzer II, CA, USA) using QDs fluorescence with cell tracker and then confirmed results by confocal microscopy (CLSM Zeiss LSM 800, Oberkochen, Germany). Nanoparticle adsorbed to RBC was confirmed using SEM (Zeiss FESEM Supra 55VP, Zeiss FESEM Ultra 55). Briefly, the MIOs adsorbed RBCs were first fixed with mixture of glutaraldehyde (25% wt., Sigma-Aldrich) and paraformaldehyde (95%, Sigma-Aldrich) in 1 M cacodylate buffer at pH 7.4, 4 °C for 24 h. Red blood cells were then washed serveral times in the cacodylate buffer and in the series of graded ethanol to dehydrate. Samples were further incubated with several graded hexamethyldisilazane (HMDS, 99%, Sigma-Aldrich) and finally coated onto poly-L-lysine-treated coverslips. To further confirm the amount of MIO bound to RBC surface, the supernatants from washing steps were collected hemolysis to remove the uncoupling RBC. The particle concentration was then analyzed using dynamic light scattering (DLS, Nano-ZS, Malvern, UK).

2.4. Characterizations

The morphologies of MIOs were examined using scanning electron microscopy (SEM, Hitachi SU8010). The particles were dispersed in pure ethanol and dried on the coverslips and sputter deposited with platinum in 20 mA for 90 s for SEM analysis. The crystal dimensions and composition evaluation of particles were determined by a Bruker D8 Advance X-ray diffractometer (XRD, Bruker, USA) over the 2θ range of 10 to 90^0. FTIR spectrum of MIOs was identified the functional groups of the materials by Fourier transform infrared spectrophotometer (FTIR, PerkinElmer) from 400 to 4500 cm^{-1}. The thermogravimetric analyses (TGA) were carried out to confirm the thermal degradation properties and weight loss of the samples in a temperature to 1000 °C, at heating rate 10 °C/min, and under N_2 atmosphere, using a Mettler Toledo thermogravimetric analyzer (DSC/TGA 3+ Star, Greifensee, Switzerland). The Brunauer-Emmett-Teller surface area is evaluated by N_2 adsorption-desorption isotherms using a surface area and porosimetry system (ASAP 2020, Micromeritics). Nanoparticle size and surface charge were performed by using dynamic light scattering (DLS, Nano-ZS, Malvern, UK). For field-dependent magnetization property analysis, superconducting quantum interference device (SQUID, Quantum Design MPMS-XL7, USA) was carried out from −10,000 to 10,000 Oe at 300 K. The magnetic thermal profile was confirmed by alternating magnetic field (AMF, power cube 32/900, President Honor Industries) at a strength of 4 kA/m and frequency of 50 kHz is applied to induce the magnetic thermal effect of different particles. The solution containing 0.8 mg/mL of nanoparticles was set in the coil of MF and been heated at the altitude of 70% for 10 min continuously, and the temperature were determined by a thermal couple.

2.5. Erythrocyte agglutination by MIO particles

The method for the agglutination assay of RBC by MIO was referred to the literature [49,50]. In brief, RBC and MIO@RBC suspensions at 1% hematocrit were dispensed into each of the wells in 96 well plates, and were then incubated at 37 °C. After 1 h, the RBC and MIO:RBC suspensions were observed by using Nikon microscope.

2.6. Erythrocyte osmotic fragility

Osmotic stress assay was determined as previously studies [51,52]. Briefly, the fresh RBC and RBC:MIO suspensions at 1% hematocrit were incubated in various salt concentrations (0–200 mM) at 37 °C for 5 min. Next, the supernatant were immediately collected by centrifuging at 13400 *g* for 4 min. The osmotic results were obtained by measuring the supernatant absorbance using a plate reader (Synergy HT Multidetection microplate reader, BioTek Instruments, Inc., USA) at 540 nm.

2.7. Cellular uptake, distribution, and cytotoxicity

To evaluate the cell uptake effects and cell-cell interaction, the MIOs and MIO@RBC with different concentration were co-cultured with B16F10 (a murine tumor cell line; murine melanoma cells) cells. In brief, B16F10 cells were seeded at 37 °C in Dulbecco's modified eagle medium (DMEM), which was supplemented with 10% fetal bovine serum (FBS, Standard, Gibco) and 1% penicillin/streptomycin (10,000 U/mL, ThermoFisher Scientific), in a relative humidified 5% CO_2-enriched environment. After 24 h incubation, both particle groups were co-cultures with the B16F10 cells for different densities. The cytotoxicity assay of MIOs and MIO@RBC was investigated by a plate reader (Synergy HT Multidetection microplate reader, BioTek Instruments, Inc., USA) approach, which was incubated 10–15 min with 10 μL per well of MTT Presto blue solution (PrestoBlue™ Cell Viability Reagent, ThermoFisher Scientific), and the expressing of cell viability effects were examined at a wavelength number of 570 nm.

For imaging tracking, Quantum dots (QDs, excitation at 560 nm and emission at 610 nm) were employed to label nanoparticles. First, 20 μg/mL of QDs was loaded into the different concentration particles, and the excess QDs were washed with ethanol and PBS. The QDs loaded particles were then emerged in PBS for later using. For cell uptake study, the biomimetic NPs were cultured with B16F10 cells, which were seeded on glass coverslips for 24 h at 37 °C in advance. After incubation for various time points (or various particle densities), the staining method was carried out by removing the medium from the cells, washing with PBS, and fixing with 3% formaldehyde (PBS solution) for 30 min. The cells were then stained with 0.1% Triton X-100 (PBS solution) and washed again with PBS for performing permeabilization. The nuclei and actin cytoskeleton were further stained for 30 min with DAPI (1 μg//mL, D1306, ThermalFisher Scientific, Germany) and F-actin (300 units/mL), respectively. Finally, the cells were allowed to mount on glass slides and observed by CLSM (Zeiss LSM 800, Germany).

For quantification of the cellular uptake, B16F10 cells (1×10^5 cells) were cultured into 6-well plates. After seeded for 24 h, various particles labeled with quantum dots (QDs) were added in the well for different time duration respectively to observe the cell uptake. Then, the cells were washed by PBS, and then, treated with trypsin-EDTA. The treated cells were re-suspended into DMEM solution with 10% FBS and 1% penicillinstreptomycin. The cells were then centrifuged at 800 rpm for 5 min, and carefully re-suspended with PBS. Furthermore, the flow cytometry (BD FACSAriaTM II flow cytometer) analysis was measured to quantify the amount of particle uptake by cells, and the values were then evaluated by the FlowJo software (FlowJo 7.6, Tree Star).

2.8. Multicellular spheroids chip fabrication

The multicellular spheroids chip was prepared by poly (methyl methacrylate) (PMMA, Sigma-Aldrich) through laser cutting method. The microfluidic hanging drop chip was designed with 96 opening wells and 1.0 mm in diameter each well. The microfluidic chip was composed two layers, which are assembled by the 3 M double adhesive tape with 500 μm in depth for each layer. The bottom layer was then coated with poly(2-hydroxyethyl methacrylate) (pHEMA, BioReagent, powder, suitable for cell culture) which was dissolved in an ethanol solution (60 mg/mL in 95% ethanol). To improve the coating quality and cell formation efficiency, the bottom coverslip substrate was firstly oxygen plasma treatment treated to increase its hydrophilicity and then added 100 μL of pHEMA solution homogeneously. Afterward, the top cover and the bottom microchannel replicas were aligned and joined by oxygen plasma treatment, and then put in a conventional oven at 65 °C for 24 h to achieve permanent bonding to obtain a complete multicellular spheroids chip.

3. Results and discussion

3.1. Binding efficiency of MIOs to RBCs

MIOs were successfully synthesized by a facile ligand-assisted synthesis approach (Fig. S1a), which using sodium citrate (NaAc) and oleic amine (OA) as co-precipitated agents in the hydrothermal reaction [27]. After the hydrothermal reaction at 220 °C for 6 h, MIOs are almost uniform with an average diameter of approximately 150 nm (polydispersity index was 0.19 ± 0.043) (Fig. S1b). The primary nanoparticles (Fe_3O_4) are first formed *via* dehydration, and then the oriented growth of primary iron oxide nucleation occurs in ethylene glycol (Fig. S1b-m). With increased the reaction temperature, the increase of particle size was also observed (Fig. S1l).

In Fig. S1n-o, the results of a superconducting quantum interference device (SQUID) showed that all the particles possessed a nearly identical shape and a smooth hysteresis. The material of X-ray diffractometer (XRD) exhibited crystalline characteristic with the XRD diffraction peaks of 2 theta at 30.1°, 35.6°, 43.2°, 53.5°, 57.1° and 62.8° (Fig. S1p), which are typical planes of magnetite Fe3O4 crystal [53]. FTIR analysis in Fig. S1q had the adsorption of peak at 1595 and 2342 are due to vibration of N—H and C—H bonds, respectively. The sharp peak at 568 cm^{-1} correspond to characteristic Fe—O stretching, which is confirmed the presence of magnetite [54,55]. Fig. S1r exhibited the meso-macroporous characteristic of MIO [56,57]. TGA analysis indicated that the weight loss ratio of MIOs is approximately 9.8% (Fig. S1s). A rapid increase in temperature was observed upon an AMF irradiation (Fig. S2). The temperature of all the particle solutions increased to around 50 °C within two min of AMF treatment. The mechanism of AMF inducing heat is owing to the magnetic energy dissipation, caused by Brown and Néel relaxations [58,59].

There are two main strategies to develop RBC drug delivery have

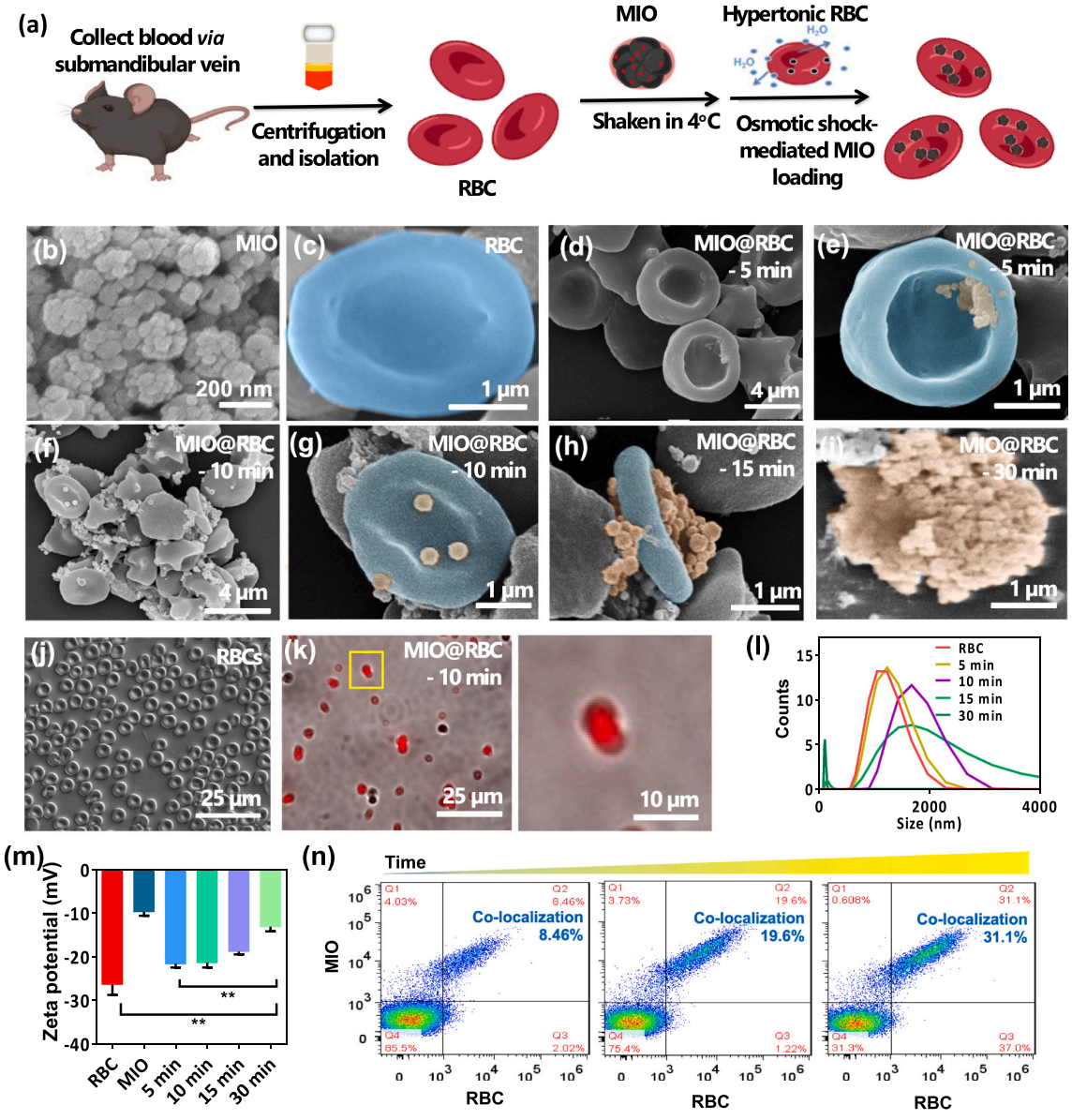

Fig. 2. Preparation and physicochemical characterization of MIO@RBC. (a) Schematic illustration of the main steps in the adsorption of MIOs on RBC. (b-i) SEM images of MIO and MIO@RBC at various shaking time of 5 min to 30 min, respectively. The fluorescence images of (j) RBC and (k) MIO@RBC were captured by using confocal microscopy. MIO was labeled by QDs and absorbed on RBC surface at 10 min. (l) Size distribution and (m) zeta potential of MIO@RBC determined by DLS at various shaking time duration (5, 10, 15 and 30 min). Error bars represent mean ± s.d., $n = 6$. $^{**}p < 0.05$ compared with the group by one-way ANOVA with Tukey's multiple-comparison test. (n) The co-localization of MIO and RBC with different time of interaction. The co-localization experiments were performed by flow cytometry, RBC and MIO were labeled by DiI and Cy5.5, respectively.

been employed for several decades. First strategy involves encapsulation of a drug into isolated RBCs. The cargoes encapsulated into inner volume of RBCs during osmotic swelling *via* transient pores in the RBC ghosts, and hypotonic treatment [60,61]. Additionally, the recent strategy is coupling cargoes to RBC, which is to physically absorb onto the RBC surface [52,62,63]. This approach is referred to as 'RBC hitchhiking' and revealed the effectiveness of overcoming challenges to NPs-based therapy. Based on our design and results, it is believed that the cargoes have absorbed onto RBC surface *via* non-specific absorption, hydrophobic interactions, electrostatic forces, hydrogen bonding and Van der Waals forces [26]. Moreover, the reversible non-covalent bonds between cargoes and RBC were further enabling the release mechanism for loaded NPs [59]. In this study, the MIOs absorbed to RBC were investigated *via* coupling to RBC approach and evaluated by incubated at various times to find the optimal adsorbed conditions. RBCs were collected from black female mice (6 to 8 weeks old) *via* submandibular vein and washed in phosphate buffered saline (PBS, pH 7.4, Gibco, 10010023) for several times to remove the serum. Then, the RBCs were mixed with MIOs and constantly shaken for 5 to 30 min at 4 °C (Fig. 2a). The SEM images revealed the effectiveness of MIOs absorbed to RBCs by time shaking from 5 to 30 min. As shown in Fig. 2b to 2i, the morphologies of RBC were deformed when the shaking time longer than 30 min. With 10 min of interacting, the well-distributed MIOs were deposited onto RBC (Fig. 2f and g). The morphology of MIOs was kept on RBC under SEM image, indicating that the MIOs didn't totally fuse into the RBCs and RBCs maintain the intact structure. With longer time of shacking, the high coverage and aggregation of MIOs on RBCs were observed (Fig. 2h and i). To track the loading efficiency, MIO was labeled by DiI (a fluorescent lipophilic cationic indocarbocyanine dye, also known as $DiIC_{18}$; excitation at 565 nm and emission at 595 nm). The fluorescence images of MIO@RBC indicated that more the 70% of RBCs possessed IOs (Fig. 2j–k). Furthermore, while coating onto the RBC surface, the MIO changed the size and surface charge of fresh RBC (Fig. 2l–m). The dimensional stability of MIO absorbing on RBC surface has been completely recorded for 8 days (Fig. S3). The dimensional stability of MIOs on RBC assessed by DLS showed that the structure and distribution of RBC-MIO is good after 8 days (Fig. S3a–S3b) The co-localization of MIO and RBCs increased with time (Fig. 2n). After 15 min of incubating, the co-localization efficiency was higher than 30%.

To quantify the amount of MIO bound to RBC, the particle concentrations were estimated by Nanoparticle tracking analysis (NTA, Malvern, UK). The NTA system uses a laser to illuminate the particles in a sample and tracks their movement using Brownian motion. This system was used to assess the amount of MIO before and after erythrocyte adsorption (fixing RBC concentration at 1×10^6 red blood cells). As shown in Fig. S3c–d, ~80% of MIO was bound to the RBC surface after the centrifugation process. The number of MIOs on each RBC is about 19.

To further evaluate the effect of MIO on mouse erythrocytes, a series of *in vitro* experiments including hemagglutination and osmotic fragility of erythrocytes were performed. These assays were performed in 96-well plates with a 1% hematocrit of RBC solution, which is common in manual testing [50]. As shown in Fig. S3e, at NaCl concentrations below 40 mM, the erythrocyte osmotic fragility curves did not change between the MIO dilution groups. Furthermore, the effect of MIO binding on the sensitivity of RBCs to osmotic lysis at hypotonic NaCl concentrations at NP/RBC ratios ranging from 50:1 to 200:1 did not alter hemolysis in mice at rate-limiting osmolarity (*e.g.*, 75 mM NaCl), However, NP loading at a NP/RBC ratio of 500:1 aggravated osmolysis in mice. Since the amount of MIO required to couple RBCs and trigger agglutination is unknown, agglutination assays were performed with different MIO dilutions. The results from Fig. S3f and S3g show that agglutination was observed in the two highest ratios of MIO/RBC after 5 min of incubation, but had no effect on RBC agglutination at MIO concentrations below 200 mg/mL.

3.2. Cytotoxicity and cell uptake of MIO@RBC

The cell uptake of MIO and MIO@RBC was evaluated by co-culturing particles with B16-F10 cells (a murine tumor cell line; skin melanoma cells). After incubation of B16-F10 cells with MIO and MIO@RBC, it was detected that both red fluorescence overlapped around the nuclei (Fig. 3a and Fig. S4a). The free MIOs were gradually uptaken by the cells after 20 min exposure time and this further increase for 4 h incubation. The mechanism could be understood by the endocytosis of cancer cell, and the cancer cells snatched MIOs from RBCs. During the co-incubating process, most RBCs were not uptaken by other cells owing to the CD 47 as a "self-marker" on cell membranes that signals the phagocyte receptor CD172a and inhibits the immune response [64]. The quantification was confirmed by flow cytometry was applied and shown in Fig. 3b.

In vitro cell cytotoxicity of MIO@RBC (MTT assay) was evaluated by co-culturing particles with B16-F10 cells for 24 h at various concentrations to evaluate the safety of nanoparticles initially. In Fig. S3b, the cell viability was maintained higher than 80% at various concentrations of free MIOs, which predicted the low toxicity. Moreover, after depositing on RBC, the toxicity slightly reduced, suggesting the high biocompatibility of MIO@RBC. However, the cell viability of 30 min-shacking of MIO@RBC at 20 μg/mL was around 60%, and it attributed by the oxidative stress of MIO@RBC Furthermore, the intensity of MIO signals was confirmed by using ImageJ software (Fig. S3c).

3.3. Penetration of MIO@RBC in tumor spheroids

RBCs can be used as natural carriers for nanoparticle-based drug delivery systems, a concept known as "hitchhiking" delivery. The advantage of this approach is that RBCs can pass through the body's vascular system and transport drug-loaded nanoparticles to tumors, which are known to have leaky vasculature. Tumor spheroid studies provide an opportunity to test the efficacy of hitchhiking drug delivery systems in a three-dimensional environment that better mimics the *in vivo* conditions. In this context, RBCs can be used to deliver nanoparticles to spheroids, which can then be used to study the distribution and penetration of nanoparticles in the tumor microenvironment. These studies can help researchers optimize the design of nanoparticle-based drug delivery systems by assessing their ability to penetrate tumor tissue and deliver therapeutic payloads to cancer cells while minimizing toxicity to healthy cells. Furthermore, the use of RBCs as natural carriers can potentially overcome the problem of clearance by the immune system, resulting in prolonged circulation times and improved therapeutic outcomes.

To investigate the penetration of the particles into the tumor spheroid, a multicellular tumor spheroid (MTS) on a microfluidic chip was examined. The 3D tumor spheroid was developed by co-culturing B16F10 cells and NIH/3 T3 cells (mouse embryonic fibroblasts) with volume ratio 2:1 on microfluidic chip (Fig. 3c) [65]. After 48 h of incubation, the uniform tumor spheroids with 200 μm on a chip could be observed (Fig. 3d). The high magnification of CLSM image of tumor spheroid indicated the compact cells with a clear cell boundary in the spheroid (Fig. 3e). The cell cytotoxicity of MIO@RBC showed that MIO and MIO@RBC exhibited the low toxicity and good biocompatibility for NIH/3 T3 cells (Fig. 3f).

To evaluate the penetration and release in MTS, MIO and MIO@RBC were injected onto the chip at a constant rate of 100 μL/min. The CLSM images exhibited the particles attached on spheroids at 4 h post-treatment, and most particles were observed inside the MTS for MIO group (Fig. 3g and S5). However, most of MIO@RBC resided in the surrounding of the MTS at 4 h post-treatment. With time increasing to 24 h, the inner region of MTS appeared the accumulation of particles. The penetration and accumulation of particles into the inner regions of the MTSs was probably induced and weakened cell–cell interactions, known as nanoparticle-induced extracellular leakiness (nanoEL) [35]. The results also indicated that the MIOs could be transferred from

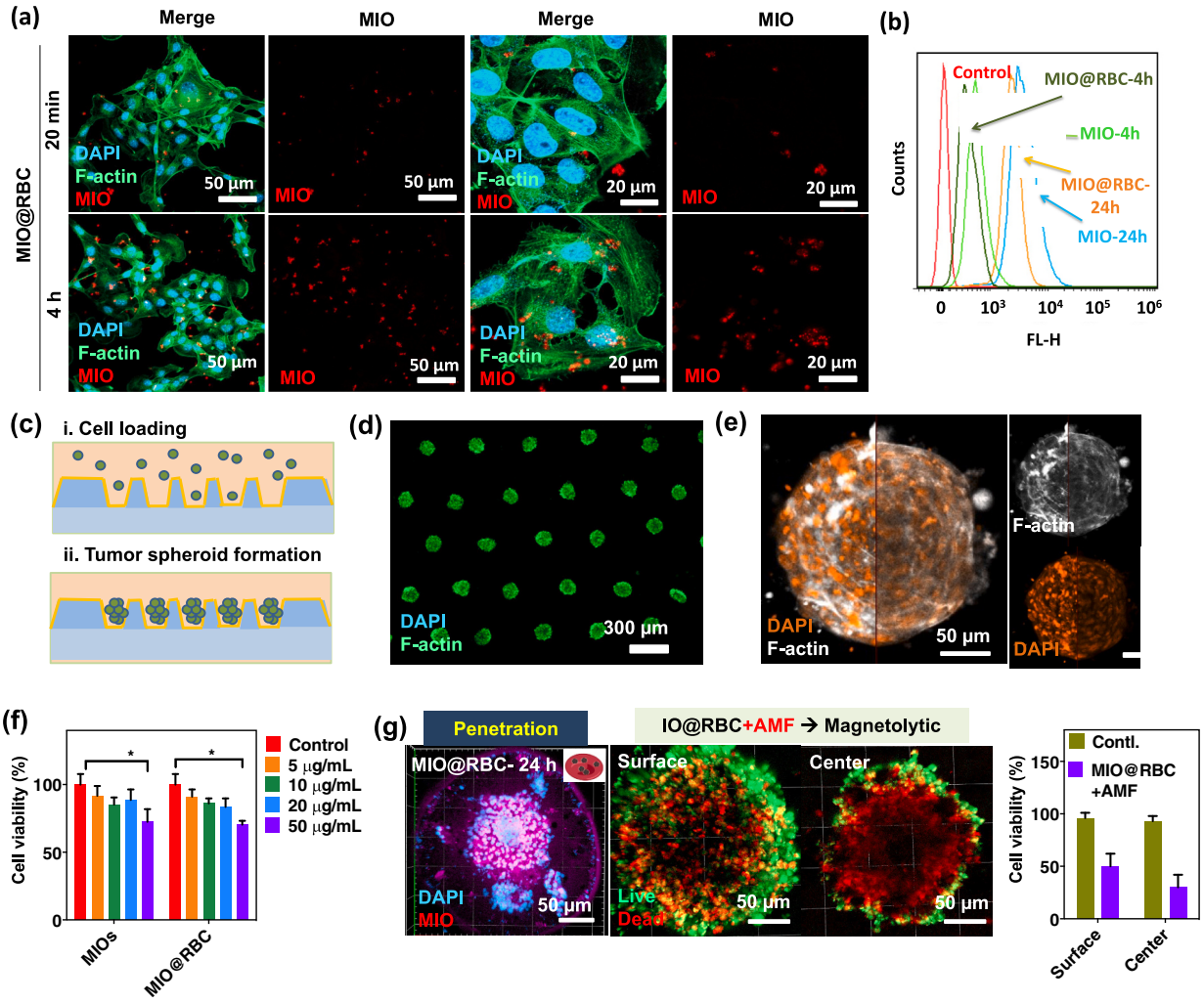

Fig. 3. (a) Confocal images of cell uptake of B16F10 cells incubated with MIO@RBC at 100 μg/ mL of concentration for 20 min and 4 h. Blue and green signals exhibited nucleus labeled with DAPI and cytoskeleton labeled with F-actin, respectively. MIO labeled with QDs represented in red. (b) Flow cytometry analysis of MIO and MIO@RBC after 24 h of incubation in B16F10 cells. To track the cell uptake efficiency, MIO was labeled by QDs. (c) The preparation of a multicellular tumor spheroid (MTS) on a microfluidic chip *via* co-culturing B16F10 cells and NIH/3 T3 cells (mouse embryonic fibroblasts). (d, e) CLSM images of MTSs untreated (control), nuclei are displayed in blue, and F-actin is exhibited in green. (f) Cell viability of NHI/3 T3 cells with MIO and MIO@RBC. Error bars represent mean ± s.d., n = 6. *$p < 0.1$ compared with the group by one-way ANOVA with Tukey's multiple-comparison test. (g) CLSM images of MTSs treated by MIO@RBC with or without 1 min of AMF treatment. The particles were labeled with DiI represented in red fluorescence. Live/dead images of MTS after treated by MIO@RBC with and without AFM. (For interpretation of the references to colour in this figure legend, the reader is referred to the web version of this article.)

MIO@RBC to MTS *via* the endocytosis of cancer cell and the cancer cells snatching MIOs from RBCs. Furthermore, while subjecting to an AMF (at a power of 3.2 kW and frequency of 50 kHz), the magnetothermal effects led the effective cell death for MIO@RBC + AMF groups (Fig. 3g). The dead cell could be observed inside the MTS.

3.4. *In vivo* lung accumulation of MIO@RBC

The RBC-hitchhiked MIO in lung metastasis was performed *in vivo*. The formation of numerous metastatic foci in the lung was obtained intravenously 14 days after the injection of GFP-B16F10 cells (Fig. S6). To compare the MIO accumulation at lung, mice were treated with PBS, MIO and MIO@RBC *via* the tail vein (IV injection), and major clearance organs were obtained at 24 h post-injection. The fluorescence of harvested organs was evaluated by IVIS Spectrum *in vivo* imaging system (Fig. 4a). For saline group, the fluorescence of liver was raised from the autofluorescence background of liver. RBC-hitchhiked MIO was capable to increase the MIO delivery to the lung. However, in the absence of erythrocyte trafficking, MIO accumulates in the liver primarily through a process called uptake by the reticuloendothelial system (RES).

To further confirm the lung accumulation of RBC hitchhiked nanoparticle, mice were treated with PBS, MIO and MIO@RBC *via* intra-arterial (IA) injection, and the clearance organs were obtained at 24 h post-injection. Compared to IV injection, IA injection routing to first pass in large vascular bed like mesenterial or cerebral was applied to estimate the hitchhiking lung delivery. As shown in Fig. 4a, the results indicated that both IV and IA injection displayed the effective lung accumulation for MIO@RBC groups while compared to MIO alone, suggesting the efficacy of RBC-hitchhiked MIO. The main reasons can be drawn as follows. First, the lung has a highly developed capillary network, providing a large surface area for efficient drug delivery. RBCs can deliver nanoparticles to the lung capillaries and facilitate their entry into the lung tumor. Second, RBCs can shield the nanoparticles from the immune system and decease accumulation in spleen and liver [28]. Furthermore, when red blood cells squeeze through the narrow capillaries of the lungs, the red blood cells can adhere to the endothelial cells lining the tumor blood vessels and transfer the nanoparticles to the endothelial cells [26,62].

The *in vivo* co-localization between MIO and metastasis lung cells (GFP-B16F10 cells) was verified to compare the capability of

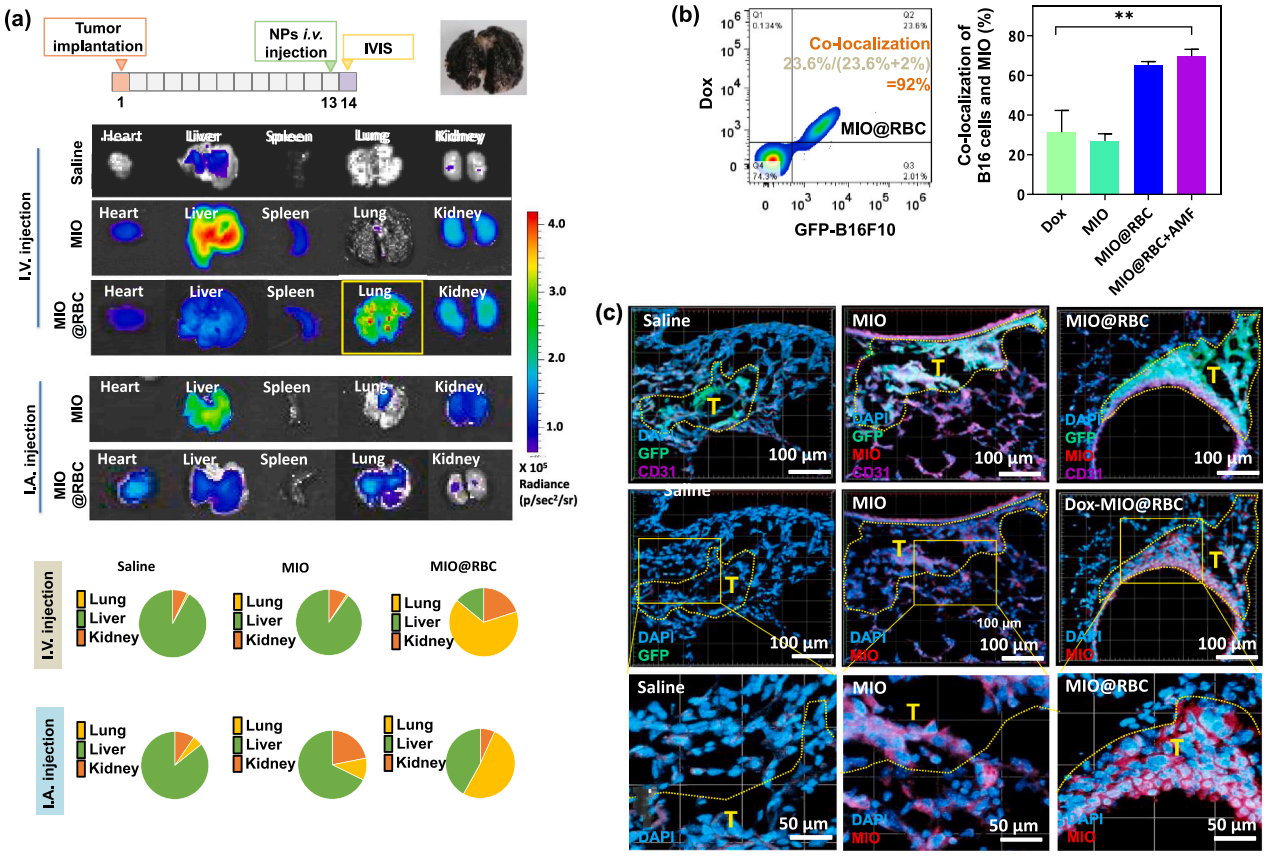

Fig. 4. *In vivo* study of mice bearing B16F10 lung metastases treated with free MIO and MIO@RBC. (a) IVIS images of lung after treated saline (control group), MIO and MIO@RBC *via* intravenous and intra-artery injection at 24 h posttreatment. (b) Co-localization of GFP-B16F10 and MIOs by using flow cytometry. Error bars represent mean ± s.d., n = 6. $^{**}p < 0.05$ compared with the group by one-way ANOVA with Tukey's multiple-comparison test. (c) Confocal images of mice bearing GFP-B16F10 lung metastases after treated with MIO and MIO@RBC after 24 h of treatment, respectively.

recognizing cancer cells of the treatment groups by flow cytometry analysis (Fig. 4b and S7). Doxorubicin (Dox, excitation at 470 nm and emission at 560 nm) was applied as the model drug to estimate the colocalization of B16F10 cancer cells and MIO *in vivo* [66]. The disseminated single cells harvested from metastases lung organs were examined. It can clearly be seen that MIO@RBC + AMF group highly associated with GFP-expressing cancer cells, which achieved approximately 92% co-localization. Furthermore, the co-localization between MIO and metastasis lung cells (GFP-B16F10 cells) was evaluated by the lung slices. Based on the fluorescence intensity, the results also showed that >65% of co-localization between MIO and metastasis lung cells was obtained, suggesting that the RBC hitchhiking was able to identify the diseased mice lungs with ideal accuracy.

The *in vivo* targeting effects of RBC and MIO on lung metastasis were investigated in mice bearing B16F10 lung metastases. For tracking purposes, MIO and RBC were labeled in advance with CdSe quantum dots (QDs, emission at 530 nm) and Dil (emission at 595 nm), respectively. The organ accumulation of these three MIO and RBC was evaluated by the quantitative determination of Cd in each clearance organ by ICP-MS and fluorescence intensity (IVIS), respectively. As shown in Fig. S8a, both MIO and RBC showed major accumulation in the lungs 24 h after injection. After 48 h of injection, most of the MIO could still reside in the lungs, but red blood cell signals appeared in the liver and kidneys. The results indicated that the detachment of MIO occurred in the lung, which was also consistent with the images of organ slices. Furthermore, Fig. S8b shows that MIO@RBC has better blood retention than MIO. MIO@RBC exhibited ~22% retention at 4 h post-injection, while MIO showed ~8% retention after a similar time period.

Additionally, Fig. 4c presented the confocal images of lung metastases *in vivo* in mice bearing GFP-B16F10 lung metastases after intravenously injecting PBS (control group), MIO and MIO@RBC at 24 h post-injection. In the control group, the fluorescence images exhibited the green fluorescence of GFP-B16F10 lung metastasis. The overlap of the red and green fluorescence in treated lung mice revealed that the accumulation of the MIO@RBC at the metastasis more targeting than that of single of MIO, indicating enhancement targeting accumulation. Tumor cells can seize particles from erythrocytes through various mechanisms such as phagocytosis, micropinocytosis, and cell-to-cell interaction [67,68]. (1) Tumor cells can engulf erythrocytes *via* phagocytosis, which involves the formation of a phagosome around the particle and subsequent fusion with lysosomes for degradation. (2) Tumor cells can also take up erythrocytes by a process of micropinocytosis, which could form small vesicles that internalize extracellular fluid and particles. (3) Tumor cells interact with erythrocytes through direct cell-to-cell contact, leading to the internalization of particles by the tumor cells.

3.5. *In vivo* mice bearing lung metastasis treated by MIO@RBC

Having demonstrated the lung accumulation, the therapeutic effects of MIO@RBC delivery system was evaluated by injecting particles to mice bearing GFP-B16F10 lung metastases. Dox was loaded into MIOs to enhance the therapeutic effect of each NPs group (The loading capacity of Dox in MIOs were approximately 0.82 mmol g^{-1}). Fig. 5a displayed the tumor foci after 14 days of tumor implantation and treated with RBC-hitchhiking nanoparticles at Day 7. Compared to the control group,

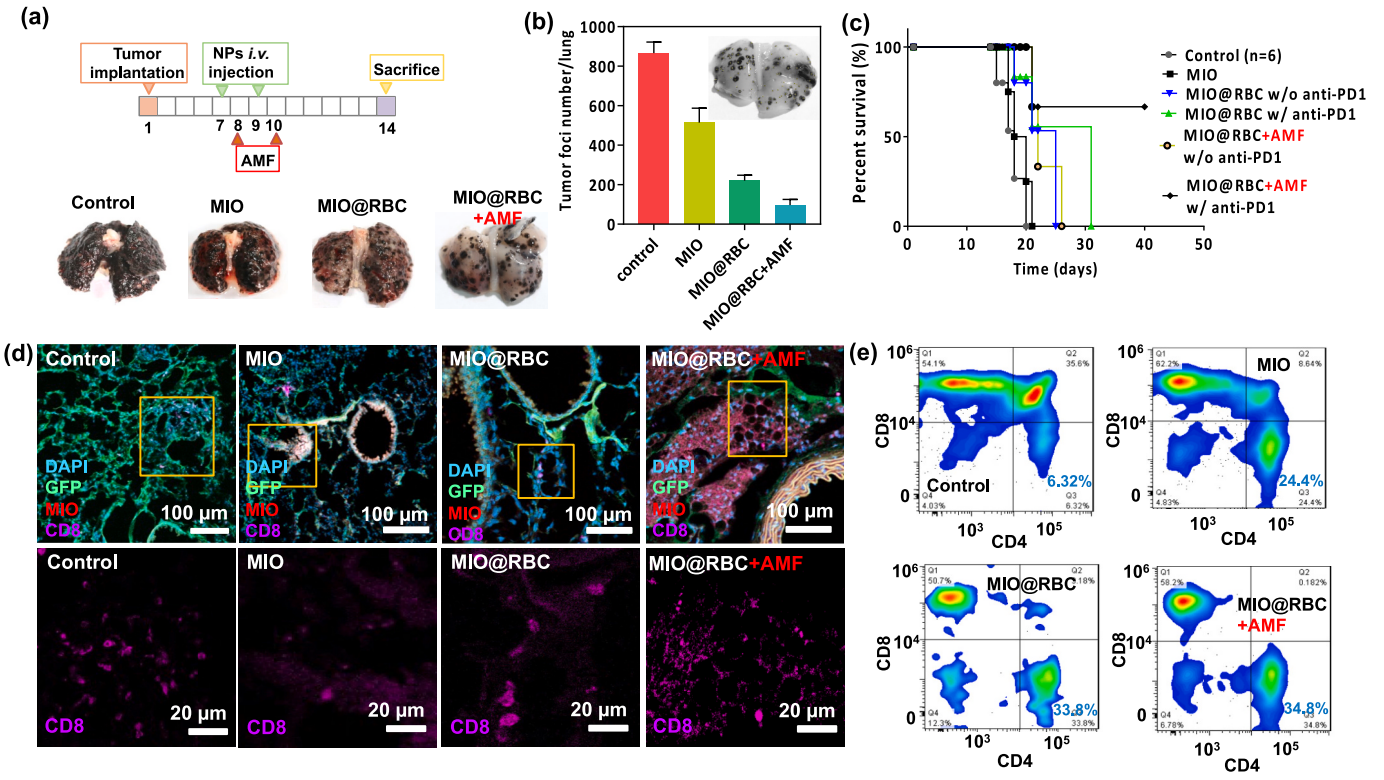

Fig. 5. *In vivo* study of mice bearing B16F10 lung metastases treated with MIO and MIO@RBC. (a) Images and (b) foci number of dissected lung metastases treated with PBS (control), MIO, MIO@RBC and MIO@RBC + AMF intravenously at 14 days postinjection, and the number of tumor foci were counted by Image J. MIO was loaded with doxorubicin (Dox). (c) Animal survival patterns of mice bearing GFP-B16F10 lung metastases treated with MIO, MIO@RBC, MIO@RBC w/ anti-PD1, MIO@RBC + AMF, and MIO@RBC + AMF with anti-PD1 for 40 days (n = 6). (d) Confocal images of mice bearing B16F10 lung metastases after treated with MIO and MIO@RBC through the tail vein, and measurement of CD 8^+ T cell. Blue and green signals exhibited nucleus labeled with DAPI and GFP-B16F10 cells, respectively. MIO labeled with Dox represented in red. $CD8^+$ represented in purple. (e) Patterns of flow cytometry showing the $CD4^+$ and $CD8^+$ expression of T cells in lungs after various treatments at 24 h postinjection. (For interpretation of the references to colour in this figure legend, the reader is referred to the web version of this article.)

the tumor foci number of treated mice decreased. Due to drug accumulation in the lungs, mice treated with MIO@RBC showed high efficacy in reducing the number of tumor foci. After calculation and counting by ImageJ software, there were about 800 tumor foci in control group, while the tumor foci decrease to 270 and 50 for lung mice treated with MIO@RBC without and with AMF, respectively (Fig. 5b). The effects on tumor suppression also reflected to the survival rate of B16F10 tumor-bearing mice. In Fig. 5c, the survival rates were monitored for up to 40 days after the mice treated with MIOs, MIO@RBC, MIO@RBC + αPD-1 and MIO@RBC + αPD-1 + AMF. The median survival rate of the control group was only around 20 days. Once the mice were treated with MIO@RBC-based groups, the results exhibited the prolonged median survival times. To improve the activating proliferation and survival signaling pathways, the mice were further treated with αPD-1. The results showed that the mice treated with MIO@RBC + αPD-1 + AMF presented effectively prolonged survival time, indicating that the AMF induced the antigen release *via* magnetothermal effect in the metastases, facilitating the immunotherapy. However, the absence of anti-PD-1 decreased the survival time.

To clarify the immune responses, the recruitment and infiltration of lymphocytes were evaluated at the lung metastases. After the lung metastasis-bearing mice was treated by various particles for 24 h, the lung was harvested, sliced and immunostaining to verify the cell population, in which the immune activity, $CD4^+$ helper T cells and $CD8^+$ cytotoxicity T cells in the lung were examined (Fig. 5d). The CLSM images demonstrated that MIO@RBC + AMF group elicited the numbers of T cells at tumor including both $CD4^+$ and $CD8^+$ T cells. It was further confirmed by the flow cytometry analysis (Fig. 5e). Gating strategy of T cells in flow cytometry was offered in Fig. S9. These results also revealed the percentage of $CD8^+$ T cells in MIO@RBC group significantly increased, and this number also increased when applying an AMF to the lung (Fig. S10).

To characterize MIO in DC, inguinal lymph nodes were harvested from mice bearing lung metastases after 24 h of treatment with saline, MIO, MIO@RBC, and MIO@RBC + AMF. The T cell subsets of LN single cells were stained and identified using the fluorochrome-conjugated anti-CD86. As shown in Fig. S11, the results of flow cytometry indicated the signals of particles from MIO on DC, which is consistent with the CLSM images of LN. Furthermore, the degree of DC maturation in lymph nodes was evaluated using the expression of CD11c and CD86.

To assess the extent of DC maturation in LNs, inguinal, cervical, and axillary LNs were collected from mice bearing lung metastases that were sacrificed 24 h after various treatments. T cell subsets of LN single cells were stained and identified using anti-CD86 (FITC-65068, Proteintech) and CD11c monoclonal antibodies (APC-65130, Proteintech). The results exhibited an increased overlap between CD11c and CD86, two cell surface markers commonly used to identify mature DCs (Fig. S12). This suggests that the treatments induced DC maturation. Particles induce dendritic cell (DC) maturation through a process called antigen-presenting cell (APC) activation. Nanoparticles enter DCs through phagocytosis or endocytosis and are then processed into peptides that are presented on major histocompatibility complex (MHC) molecules on the surface of the DCs. This process activates T cells, which can then mount an immune response against the antigen. The activation of these receptors leads to the release of cytokines and chemokines, which can stimulate DC maturation and the recruitment of other immune cells.

3.6. Antigen capture and deliver by MIOs

Tumor-specific antigens (TSA) are the targets of anticancer immunity. Increase the recognition of TSA has been confirmed to improve the activation of immune therapies. In our delivery system, the effect of MIO on antigen capture and migration potentially enhanced the T cell recruitments (Fig. 6a). First, the release of neoantigens and damage-associated molecular pattern from B16F10 cells was actuated by magnetothermal treatment, and then, the released antigens were captured by MIO and MIO@RBC. The antigens from B16F10 captured by MIO and MIO@RBC were analyzed by using liquid chromatography mass spectrometry (LC-MS/MS, Orbitrap Elite™ Hybrid Ion Trap-Orbitrap Mass Spectrometer, ThermoFisher Scientific, USA). The most prominent proteins were identified (Fig. 6b), where >60 proteins in detectable quantity were found on MIO and MIO@RBC. Damage-associated molecular patterns are endogenous molecules which serve as potent activators to enhance an immune response (Fig. S13 exhibited the sample preparation and identification of proteins by LCMSMS) [69].

In these antigens, several key features of tumor-associated antigens were observed. For example, TP53, a specific neoantigen for modulating suppression of cancer cell proliferation, functions as a tumor suppressor and apoptosis [70]. Ephrin proteins (Ephs) have a critical role in regulation of the migration and adhesion of cells, exerts complex activities in cancer; EphA6 can reduce lung and lymph node metastasis *in vivo* [71]. Furthermore, actin is an ideal DAMP detected by DNGR-1 receptor usually provides structural support to the cell, and is sensed by the immune system when released from dying cells [72]. Ubiquitin is heat-stable protein in all eukaryotic cells. These antigens have been recognized as an endogenous opponent of DAMPs to modulate immune responses. The material surface has a vital role in protein adsorption onto MIOs, the formation of protein-adsorption is involved simultaneously.

Immune system can be activated by improving the recognition of tumor-derived protein antigens and fight cancer by itself. Therefore, it is proposed to use nanoparticles to capture antigens and deliver antigens to antigen-presenting cells (APCs) such as dendritic cells (DCs). DCs take antigens to lymph nodes and further activate immune system to generate T-cell immune responses. The delivery of MIOs to lymph node was tested *in vivo*. The T cell zone of lymph node was evaluated to understand the activation of dendritic cells. The T cell zone, also known as the paracortex, is the area of the lymph node where T cells interact with dendritic cells and become activated in response to antigens presented by the dendritic cells. This process is critical for the development of effective immune responses against pathogens and other foreign substances. After various treatments, in lymphatic section, MIOs overlapped with CD86, which indicated that it can be successfully captured by DCs (Fig. 6c). In addition, without the magnetolytic therapy, the accumulation of particles in lymph nodes were decreased, indicating that the DAMPs-adsorbed MIOs potentially induced the DC delivery. Fig. 6d shown the heat map representation of typical chemokine secretion, which also indicated several key features of tumor-associated antigens *via* the MIO@RBC-mediated antigen captures.

To assess particle inflammatory and immune responses, mice bearing lung metastases were sacrificed 24 h after various treatments, and blood serum was collected for the immunological evaluations post-treatment. The levels of the following immune factors were determined, including interleukin-2 (IL-2) and interleukin-12 (IL-12) using ELISA assay (DY419 and DY417, DuoSet ELISA, R&D Systems). The levels of immune factors including interleukin-2 (IL-2) and interleukin-12 (IL-12) in serum from treated mice were detected by ELISA kits (Fig. S14). Both cytokines increased after the treatments, suggesting the stimulation of an immune responses. The treatments improved IL-2 and IL-12 expression by providing a stimulus for the activation of immune cells. The introduction of antigens into the body can trigger the activation of dendritic cells, which can then produce IL-12 and stimulate the differentiation of T cells into the Th1 subset. Additionally, the activation of T cells can lead to the production of IL-2, which can further promote the proliferation and differentiation of immune cells.

4. Conclusion

A red blood cells (RBC)-hitchhiking multi-grained iron oxide nanostructures (MIOs) that can enhance the lung metastasis delivery was constructed to osmotic shocking-mediated fusion. At lung, squeezing RBC at microvessels induces the accumulation of MIO to the pulmonary

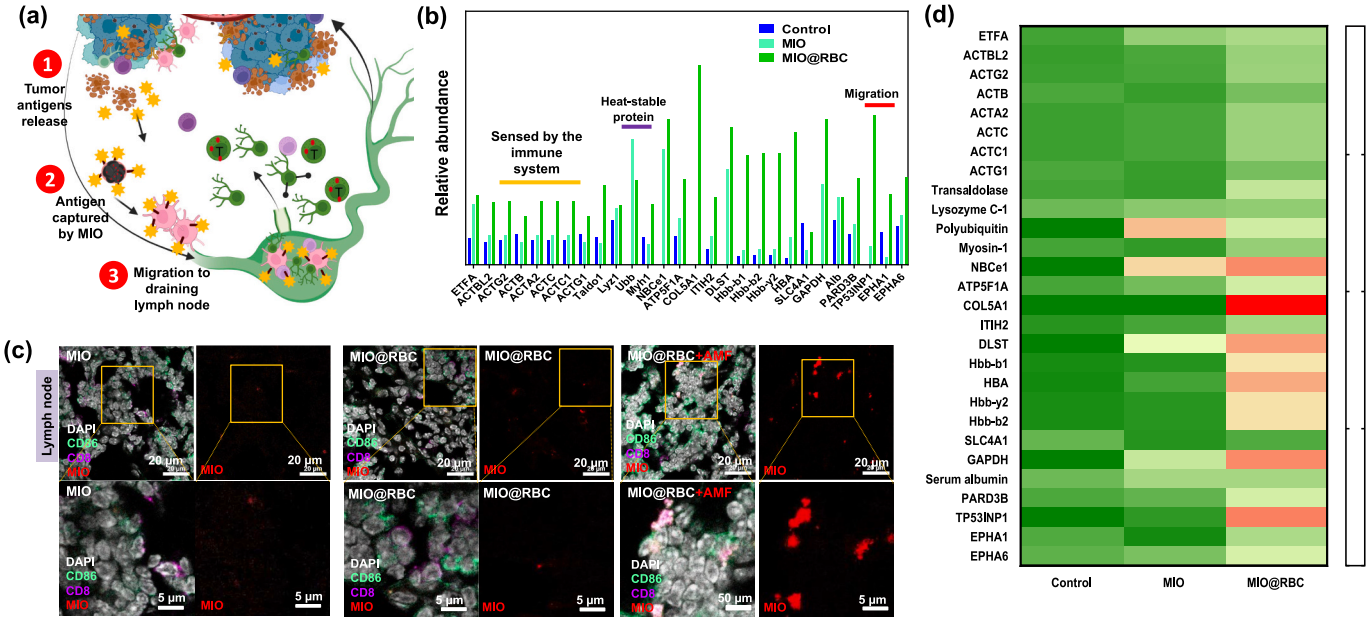

Fig. 6. (a) The MIOs were captured antigens and delivered antigens to antigen-presenting cells (APCs) such as dendritic cells (DCs). DCs take antigens to lymph nodes and further activate immune system to generate T-cell immune responses. (b) Percentage of antigens captured by MIO and MIO@RBC after AMF treatments were qualitative by LC-MS/MS. (c) Immunofluorescence staining images of CD86 in lymph nodes of mice bearing B16F10 lung metastases treated with various treatments, MIO, MIO@RBC with and without AMF at 24 h post-injection. (d) Heat map representation of typical chemokine secretion of B16F10 cells line after various treatments.

capillary endothelial cells, and >65% of MIO injected *via* the tail vein exhibited co-localized to tumors instead of normal tissue at lung due to the tumor leakage. Upon an AFM irradiation, the intense heat generated on MIO caused the cancer call apoptosis and the release of tumor-associated antigens. The MIOs can further served as an antigen capture agent to effectively deliver these antigens to lymph nodes, facilitating to effectively recruit T cells and infiltration. The role of red blood cells (RBC)-hitchhiking mediated lung metastasis delivery enhancing MIO accumulation and the activation of immune therapy leads to tumor inhibition and prolonged survival time. We expect that the hitchhiking delivery and antigen capture can provide a strategy for eliciting immune cell and suppressing tumors in the clinic.

CRediT authorship contribution statement

Thi My Hue Huynh: Investigation, Validation, Writing – original draft. **Bhanu Nirosha Yalamandala:** Investigation, Validation. **Min-Ren Chiang:** Validation. **Wei-Han Weng:** Validation. **Chien-Wen Chang:** Validation. **Wen-Hsuan Chiang:** Investigation, Validation, Formal analysis. **Lun-De Liao:** Writing – review & editing. **Yu-Chen Liu:** Formal analysis. **Shang-Hsiu Hu:** Supervision, Conceptualization, Methodology, Writing – review & editing.

Declaration of Competing Interest

The authors declare no conflict of interest.

Data availability

The data that support the findings of this study are available within the article and its supporting information.

Acknowledgements

This work was financially supported by the Ministry of Science and Technology of the Republic of China, Taiwan under contracts MOST 111-2314-B-007-003-MY3, MOST 111-2636-E-007-021 and MOST-110-2634-F-007-025, National Tsing Hua University (111Q2715E1 and 111F7MELE1) and National Health Research Institutes (NHRI-EX111-11111EI) in Taiwan.

Appendix A. Supplementary data

Supplementary data to this article can be found online at https://doi.org/10.1016/j.jconrel.2023.05.028.

References

[1] P. Sharma, S.H. Lieskovan, J.A. Wargo, A. Ribas, Primary, adaptive, and acquired resistance to cancer immunotherapy, Cell 168 (2017) 707–723.
[2] Q. Ni, F. Xu, Y. Wang, Y. Li, G. Qing, Y. Zhang, J. Zhong, J. Li, X.J. Liang, Nanomaterials with changeable physicochemical property for boosting cancer immunotherapy, J. Control. Release 342 (2022) 210–227.
[3] E. Blanco, H. Shen, M. Ferrari, Principles of nanoparticle design for overcoming biological barriers to drug delivery, Nat. Biotechnol. 33 (2015) 941–951.
[4] F. Zhang, G. Lu, X. Wen, F. Li, X. Ji, Q. Li, M. Wu, Q. Cheng, Y. Yu, J. Tang, Magnetic nanoparticles coated with polyphenols for spatio-temporally controlled cancer photothermal/immunotherapy, J. Control. Release 326 (2020) 131–139.
[5] J.A. Joyce, D.T. Fearon, T cell exclusion, immune privilege, and the tumor microenvironment, Science 348 (2015) 74–80.
[6] Y. Chao, G. Chen, C. Liang, J. Xu, Z. Dong, X. Han, C. Wang, Z. Liu, Iron nanoparticles for low-power local magnetic hyperthermia in combination with immune checkpoint blockade for systemic antitumor therapy, Nano Lett. 19 (2019) 4287–4296.
[7] J. Zhang, Y. Lin, Z. Lin, Q. Wei, J. Qian, R. Ruan, X. Jiang, L. Hou, J. Song, J. Ding, Stimuli-responsive nanoparticles for controlled drug delivery in synergistic cancer immunotherapy, Adv. Sci. 9 (2022) 2103444.
[8] S. Kunjachan, A. Detappe, R. Kumar, T. Ireland, L. Cameron, D.E. Biancur, V. Motto-Ros, L. Sancey, S. Sridhar, G.M. Makrigiorgos, Nanoparticle mediated tumor vascular disruption: a novel strategy in radiation therapy, Nano Lett. 15 (2015) 7488–7496.
[9] M. Howard, B.J. Zern, A.C. Anselmo, V.V. Shuvaev, S. Mitragotri, V. Muzykantov, Vascular targeting of nanocarriers: perplexing aspects of the seemingly straightforward paradigm, ACS Nano 8 (2014) 4100–4132.
[10] B.R. Smith, Z. Cheng, A. De, A.L. Koh, R. Sinclair, S.S. Gambhir, Real-time intravital imaging of RGD− quantum dot binding to luminal endothelium in mouse tumor neovasculature, Nano Lett. 8 (2008) 2599–2606.
[11] C.K. Frich, F. Krüger, R. Walther, C. Domar, A.H. Andersen, A. Tvilum, F. Dagnæs-Hansen, P.W. Denton, M. Tolstrup, S.R. Paludan, Non-covalent hitchhiking on endogenous carriers as a protraction mechanism for antiviral macromolecular prodrugs, J. Control. Release 294 (2019) 298–310.
[12] F. Wang, R. Zong, G. Chen, Erythrocyte-enabled immunomodulation for vaccine delivery, J. Control. Release 341 (2022) 314–328.
[13] R.B. Moyes, H. Kirch, J.R. DeLoach, Enhanced biological activity of human recombinant interleukin 2 coupled to mouse red blood cells as evaluated using the mouse Meth A sarcoma model, Biotechnol. Appl. Biochem. 23 (1996) 29–36.
[14] X. Sun, X. Han, L. Xu, M. Gao, J. Xu, R. Yang, Z. Liu, Surface-engineering of red blood cells as artificial antigen presenting cells promising for cancer immunotherapy, Small 13 (2017) 1701864.
[15] R. Wadhwa, T. Aggarwal, N. Thapliyal, A. Kumar, P. Yadav, V. Kumari, B.S. C. Reddy, P. Chandra, P.K. Maurya, Red blood cells as an efficient *in vitro* model for evaluating the efficacy of metallic nanoparticles, 3 Biotech 9 (2019) 1–15.
[16] P.M. Glassman, E.D. Hood, L.T. Ferguson, Z. Zhao, D.L. Siegel, S. Mitragotri, J. S. Brenner, V.R. Muzykantov, Red blood cells: the metamorphosis of a neglected carrier into the natural mothership for artificial nanocarriers, Adv. Drug Deliv. Rev. 178 (2021), 113992.
[17] S. Zaitsev, D. Spitzer, J.C. Murciano, B.S. Ding, S. Tliba, M.A. Kowalska, O. A. Marcos-Contreras, A. Kuo, V. Stepanova, J.P. Atkinson, Sustained thromboprophylaxis mediated by an RBC-targeted pro-urokinase zymogen activated at the site of clot formation, Blood Am. J. Hematol. 115 (2010) 5241–5248.
[18] Z. Zhao, J. Kim, V.C. Suja, N. Kapate, Y. Gao, J. Guo, V.R. Muzykantov, S. Mitragotri, Red blood cell anchoring enables targeted transduction and re-administration of AAV-mediated gene therapy, Adv. Sci. 2201293 (2022).
[19] J.S. Brenner, D.C. Pan, J.W. Myerson, O.A.M. Contreras, C.H. Villa, P. Patel, H. Hekierski, S. Chatterjee, J.Q. Tao, H. Parhiz, Red blood cell-hitchhiking boosts delivery of nanocarriers to chosen organs by orders of magnitude, Nat. Commun. 9 (2018) 1–14.
[20] Q. Fan, Q. Ma, J. Bai, J. Xu, Z. Fei, Z. Dong, A. Maruyama, K.W. Leong, Z. Liu, C. Wang, An implantable blood clot–based immune niche for enhanced cancer vaccination, Sci. Adv. 6 (2020) eabb4639.
[21] A.M. Fonseca, G. Porto, K. Uchida, F.A. Arosa, Red blood cells inhibit activation-induced cell death and oxidative stress in human peripheral blood T lymphocytes, Am. J. Hematol. 97 (2001) 3152–3160.
[22] B. Buttari, E. Profumo, R. Riganò, Crosstalk between red blood cells and the immune system and its impact on atherosclerosis, Biomed. Res. Int. 2015 (2015).
[23] A.C. Anselmo, S. Kumar, V. Gupta, A.M. Pearce, A. Ragusa, V. Muzykantov, S. Mitragotri, Exploiting shape, cellular-hitchhiking and antibodies to target nanoparticles to lung endothelium: synergy between physical, chemical and biological approaches, Biomaterials 68 (2015) 1–8.
[24] K. Ganguly, T. Krasik, S. Medinilla, K. Bdeir, D.B. Cines, V.R. Muzykantov, J. C. Murciano, Blood clearance and activity of erythrocyte-coupled fibrinolytics, J. Pharmacol. Exp. Ther. 312 (2005) 1106–1113.
[25] C. Wang, X. Sun, L. Cheng, S. Yin, G. Yang, Y. Li, Z. Liu, Multifunctional theranostic red blood cells for magnetic-field-enhanced *in vivo* combination therapy of cancer, Adv. Mater. 26 (2014) 4794–4802.
[26] P.M. Glassman, C.H. Villa, A. Ukidve, Z. Zhao, P. Smith, S. Mitragotri, A.J. Russell, J.S. Brenner, V.R. Muzykantov, Vascular drug delivery using carrier red blood cells: focus on RBC surface loading and pharmacokinetics, Pharmaceutics 12 (2020) 440.
[27] J. Li, Y. Ding, Q. Cheng, C. Gao, J. Wei, Z. Wang, Q. Huang, R. Wang, Supramolecular erythrocytes-hitchhiking drug delivery system for specific therapy of acute pneumonia, J. Control. Release 350 (2022) 777–786.
[28] L. Rossi, F. Pierigè, C. Carducci, C. Gabucci, T. Pascucci, B. Canonico, S.M. Bell, P. A. Fitzpatrick, V. Leuzzi, M. Magnani, Erythrocyte-mediated delivery of phenylalanine ammonia lyase for the treatment of phenylketonuria in BTBR-Pahenu2 mice, J. Control. Release 194 (2014) 37–44.
[29] E. Hinde, K. Thammasiraphop, H.T. Duong, J. Yeow, B. Karagoz, C. Boyer, J. J. Gooding, K. Gaus, Pair correlation microscopy reveals the role of nanoparticle shape in intracellular transport and site of drug release, Nat. Nanotechnol. 12 (2017) 81–89.
[30] Y. Chi, J. Remsik, V. Kiseliovas, C. Derderian, U. Sener, M. Alghader, F. Saadeh, K. Nikishina, T. Bale, C. Iacobuzio-Donahue, Cancer cells deploy lipocalin-2 to collect limiting iron in leptomeningeal metastasis, Science 369 (2020) 276–282.
[31] M. Chen, Y. Tan, Z. Dong, J. Lu, X. Han, Q. Jin, W. Zhu, J. Shen, L. Cheng, Z. Liu, Injectable anti-inflammatory nanofiber hydrogel to achieve systemic immunotherapy post local administration, Nano Lett. 20 (2020) 6763–6773.
[32] S. Laurent, D. Forge, M. Port, A. Roch, C. Robic, L. Vander Elst, R.N. Muller, Magnetic iron oxide nanoparticles: synthesis, stabilization, vectorization, physicochemical characterizations, and biological applications, Chem. Rev. 108 (2008) 2064–2110.
[33] Y. Zhang, Y. Xu, D. Sun, Z. Meng, W. Ying, W. Gao, R. Hou, Y. Zheng, X. Cai, B. Hu, Hollow magnetic nanosystem-boosting synergistic effect between magnetic hyperthermia and sonodynamic therapy via modulating reactive oxygen species and heat shock proteins, Chem. Eng. J. 390 (2020), 124521.
[34] S.J. Yang, C.H. Huang, C.H. Wang, M.J. Shieh, K.C. Chen, The synergistic effect of hyperthermia and chemotherapy in magnetite nanomedicine-based lung cancer treatment, Int. J. Nanomedicine 15 (2020) 10331.

[35] W.T. Shen, R.S. Hsu, J.H. Fang, P.F. Hu, C.S. Chiang, S.H. Hu, Marginative delivery-mediated extracellular leakiness and T cell infiltration in lung metastasis by a biomimetic nanoraspberry, Nano Lett. 21 (2020) 1375–1383.
[36] S. Mourdikoudis, A. Kostopoulou, A.P. LaGrow, Magnetic nanoparticle composites: synergistic effects and applications, Adv. Sci. 8 (2021) 2004951.
[37] N. Dhas, R. Kudarha, A. Pandey, A.N. Nikam, S. Sharma, A. Singh, A. Garkal, K. Hariharan, A. Singh, P. Bangar, Stimuli responsive and receptor targeted iron oxide based nanoplatforms for multimodal therapy and imaging of cancer: conjugation chemistry and alternative therapeutic strategies, J. Control. Release 333 (2021) 188–245.
[38] L.E. Low, H.P. Lim, Y.S. Ong, S.P. Siva, C.S. Sia, B.H. Goh, E.S. Chan, B.T. Tey, Stimuli-controllable iron oxide nanoparticle assemblies: design, manipulation and bio-applications, J. Control. Release 345 (2022) 231–274.
[39] S. Santra, C. Kaittanis, J. Grimm, J.M. Perez, Drug/dye-loaded, multifunctional iron oxide nanoparticles for combined targeted cancer therapy and dual optical/magnetic resonance imaging, Small 5 (2009) 1862–1868.
[40] A. Awaad, H. Takemoto, M. Iizuka, K. Ogi, Y. Mochida, A.-H. Ranneh, M. Toyoda, M. Matsui, T. Nomoto, Y. Honda, Changeable net charge on nanoparticles facilitates intratumor accumulation and penetration, J. Control. Release 346 (2022) 392–404.
[41] J.K. Patra, G. Das, L.F. Fraceto, E.V.R. Campos, M.d.P.R. Torres, L.S. Acosta-Torres, L.A. Diaz-Torres, R. Grillo, M.K. Swamy, S. Sharma, Nano based drug delivery systems: recent developments and future prospects, J. Nanobiotechnol. 16 (2018) 1–33.
[42] J. Ming, T. Zhu, J. Li, Z. Ye, C. Shi, Z. Guo, J. Wang, X. Chen, N. Zheng, A novel cascade nanoreactor integrating two-dimensional Pd-Ru nanozyme, uricase and red blood cell membrane for highly efficient hyperuricemia treatment, Small 17 (2021) 2103645.
[43] Y. Zhang, S. Ma, X. Liu, Y. Xu, J. Zhao, X. Si, H. Li, Z. Huang, Z. Wang, Z. Tang, Supramolecular assembled programmable nanomedicine as in situ cancer vaccine for cancer immunotherapy, Adv. Mater. 33 (2021) 2007293.
[44] D.S. Chen, I. Mellman, Oncology meets immunology: the cancer-immunity cycle, Immunity 39 (2013) 1–10.
[45] L. Luo, M.Z. Iqbal, C. Liu, J. Xing, O.U. Akakuru, Q. Fang, Z. Li, Y. Dai, A. Li, Y. Guan, Engineered nano-immunopotentiators efficiently promote cancer immunotherapy for inhibiting and preventing lung metastasis of melanoma, Biomaterials 223 (2019), 119464.
[46] A.V. Kroll, R.H. Fang, Y. Jiang, J. Zhou, X. Wei, C.L. Yu, J. Gao, B.T. Luk, D. Dehaini, W. Gao, Nanoparticulate delivery of cancer cell membrane elicits multiantigenic antitumor immunity, Adv. Mater. 29 (2017) 1703969.
[47] J. Meng, P. Zhang, Q. Chen, Z. Wang, Y. Gu, J. Ma, W. Li, C. Yang, Y. Qiao, Y. Hou, Two-pronged intracellular co-delivery of antigen and adjuvant for synergistic cancer immunotherapy, Adv. Mater. 2202168 (2022).
[48] J.D. Roback, C.D. Josephson, E.K. Waller, J.L. Newman, S. Karatela, K. Uppal, D. P. Jones, J.C. Zimring, L.J. Dumont, Metabolomics of ADSOL (AS-1) red blood cell storage, Transfus. Med. Rev. 28 (2014) 41–55.
[49] L.T. Ferguson, E.D. Hood, T. Shuvaeva, V.V. Shuvaev, M.C. Basil, Z. Wang, J. Nong, X. Ma, J. Wu, J.W. Myerson, Dual affinity to RBCs and target cells (DART) enhances both organ-and cell type-targeting of intravascular nanocarriers, ACS Nano 16 (2022) 4666–4683.
[50] P.M. Glassman, C.H. Villa, O.A. Marcos-Contreras, E.D. Hood, L.R. Walsh, C. F. Greineder, J.W. Myerson, T. Shuvaeva, L. Puentes, J.S. Brenner, Targeted in vivo loading of red blood cells markedly prolongs nanocarrier circulation, Bioconjug. Chem. 33 (2022) 1286–1294.
[51] D.C. Pan, J.W. Myerson, J.S. Brenner, P.N. Patel, A.C. Anselmo, S. Mitragotri, V. Muzykantov, Nanoparticle properties modulate their attachment and effect on carrier red blood cells, Sci. Rep. 8 (2018) 1615.
[52] C.H. Villa, D.C. Pan, I.H. Johnston, C.F. Greineder, L.R. Walsh, E.D. Hood, D. B. Cines, M. Poncz, D.L. Siegel, V.R. Muzykantov, Biocompatible coupling of therapeutic fusion proteins to human erythrocytes, Blood Adv. 2 (2018) 165–176.
[53] C. Yong, X. Chen, Q. Xiang, Q. Li, X. Xing, Recyclable magnetite-silver heterodimer nanocomposites with durable antibacterial performance, Bioact. Mater. 3 (2018) 80–86.
[54] P.D. Shima, Mesoporous magnetite nanoclusters as efficient nanocarriers for paclitaxel delivery, ChemistrySelect 5 (2020) 9261–9268.
[55] G. Yang, D.-Y. Wang, Y. Liu, F. Huang, S. Tian, Y. Ren, J. Liu, Y. An, H.C. van der Mei, H.J. Busscher, In-biofilm generation of nitric oxide using a magnetically-targetable cascade-reaction container for eradication of infectious biofilms, Bioact. Mater. 14 (2022) 321–334.
[56] F.J. Sotomayor, K.A. Cychosz, M. Thommes, Characterization of micro/mesoporous materials by physisorption: concepts and case studies, Acc. Mater. Surf. Res 3 (2018) 34–50.
[57] D. Feng, H. Yang, X. Guo, 3-dimensional hierarchically porous ZnFe2O4/C composites with stable performance as anode materials for Li-ion batteries, Chem. Eng. J. 355 (2019) 687–696.
[58] J.H. Lee, J.T. Jang, J.S. Choi, S.H. Moon, S.H. Noh, J.W. Kim, J.G. Kim, I.S. Kim, K. I. Park, J. Cheon, Exchange-coupled magnetic nanoparticles for efficient heat induction, Nat. Nanotechnol. 6 (2011) 418–422.
[59] C. Wang, N. Zhao, Y. Huang, R. He, S. Xu, W. Yuan, Coordination of injectable self-healing hydrogel with Mn-Zn ferrite@ mesoporous silica nanospheres for tumor MR imaging and efficient synergistic magnetothermal-chemo-chemodynamic therapy, Chem. Eng. J. 401 (2020), 126100.
[60] M. Magnani, F. Pierigè, L. Rossi, Erythrocytes as a novel delivery vehicle for biologics: from enzymes to nucleic acid-based therapeutics, Ther. Deliv. 3 (2012) 405–414.
[61] R. Sabatino, A. Antonelli, S. Battistelli, R. Schwendener, M. Magnani, L. Rossi, Macrophage depletion by free bisphosphonates and zoledronate-loaded red blood cells, PLoS One 9 (2014), e101260.
[62] R. Carnemolla, C.H. Villa, C.F. Greineder, S. Zaitsev, K.R. Patel, M.A. Kowalska, D. N. Atochin, D.B. Cines, D.L. Siegel, C.T. Esmon, Targeting thrombomodulin to circulating red blood cells augments its protective effects in models of endotoxemia and ischemia-reperfusion injury, FASEB J. 31 (2017) 761.
[63] C.H. Villa, D.C. Pan, S. Zaitsev, D.B. Cines, D.L. Siegel, V.R. Muzykantov, Delivery of drugs bound to erythrocytes: new avenues for an old intravascular carrier, Ther. Deliv. 6 (2015) 795–826.
[64] S.Y. Sung, Y.L. Su, W. Cheng, P.F. Hu, C.S. Chiang, W.T. Chen, S.H. Hu, Graphene quantum dots-mediated theranostic penetrative delivery of drug and photolytics in deep tumors by targeted biomimetic nanosponges, Nano Lett. 19 (2018) 69–81.
[65] S. Shen, G. Wang, M. Zhang, Y. Tang, Y. Gu, W. Jiang, Y. Wang, Y. Zhuang, Effect of temperature and surfactant on biomass growth and higher-alcohol production during syngas fermentation by *Clostridium carboxidivorans* P7, Bioresour. Bioprocess. 7 (2020) 1–13.
[66] M. Norouzi, V. Yathindranath, J.A. Thliveris, B.M. Kopec, T.J. Siahaan, D. W. Miller, Doxorubicin-loaded iron oxide nanoparticles for glioblastoma therapy: a combinational approach for enhanced delivery of nanoparticles, Sci. Rep. 10 (2020) 11292.
[67] Y. Feng, Q. Liu, Y. Li, Y. Han, M. Liang, H. Wang, Q. Yao, Y. Wang, M. Yang, Z. Li, W. Gong, Y. Yang, C. Gao, Cell relay-delivery improves targeting and therapeutic efficacy in tumors, Bioact. Mater. 6 (2020) 1528–1540.
[68] Z. Zhao, A. Ukidve, Y. Gao, J. Kim, S. Mitragotri, Erythrocyte leveraged chemotherapy (ELeCt): nanoparticle assembly on erythrocyte surface to combat lung metastasis, Sci. Adv. 5 (2019) eaax9250.
[69] C.F. Wenceslau, C.G. McCarthy, T. Szasz, K. Spitler, S. Goulopoulou, R.C. Webb, Mitochondrial damage-associated molecular patterns and vascular function, Eur. Heart J. 35 (2014) 1172–1177.
[70] H. Yang, L. Sun, A. Guan, H. Yin, M. Liu, X. Mao, H. Xu, H. Zhao, X. Lu, X. Sang, Unique TP53 neoantigen and the immune microenvironment in long-term survivors of hepatocellular carcinoma, Cancer Immunol. Immunother. 70 (2021) 667–677.
[71] S. Li, Y. Ma, C. Xie, Z. Wu, Z. Kang, Z. Fang, B. Su, M. Guan, EphA6 promotes angiogenesis and prostate cancer metastasis and is associated with human prostate cancer progression, Oncotarget 6 (2015) 22587.
[72] N. Srinivasan, O. Gordon, S. Ahrens, A. Franz, S. Deddouche, P. Chakravarty, D. Phillips, A.A. Yunus, M.K. Rosen, R.S. Valente, L. Teixeira, B. Thompson, M. S. Dionne, W. Wood, C.R. e Sousa, Actin is an evolutionarily-conserved damage-associated molecular pattern that signals tissue injury in *Drosophila melanogaster*, eLife 5 (2016), e19662.